Petroleum Science 23 (2026) 5960–5971

Contents lists available at ScienceDirect

Petroleum Science

journal homepage: www.keaipublishing.com/en/journals/petroleum-science

Original Paper

Optical and rheological properties of carbon quantum dots regenerated aged asphalt based on molecular simulation and experiments

Xin-Xing Zhou [a,b,*], Tian-Qi Zong [a], Ling-Lin Li [c], Seung-Soo Kim [d]

[a] Institute of Resources and Environmental Engineering, Shanxi University, Taiyuan, 030031, Shanxi, China
[b] School of Environmental Science and Engineering, Tianjin University, Tianjin, 300350, China
[c] Built Environment, Wrexham University, Wrexham, LL11 2AW, Wales, UK
[d] Department of Chemical Engineering, College of Engineering, Kangwon National University, Samcheok-Si, 25913, Republic of Korea

ARTICLE INFO

Article history:
Received 28 December 2025
Received in revised form
6 May 2026
Accepted 28 June 2026
Available online 3 July 2026

Edited by Min Li

Keywords:
Regenerated asphalt
Carbon quantum dot
Rheological property
Optical response
Molecular simulation

ABSTRACT

To investigate the rheological and optical properties of carbon quantum dots (CQDs)-regenerated aged asphalt (CQDsRA), four types of CQDs, $C_{34}H_{14}O_2$ (CQDs-1), $C_{52}H_{72}O_{14}$ (CQDs-2), $C_{39}H_{30}N_6O_{10}$ (CQDs-3), and $C_{52}H_{72}O_{10}S_4$ (CQDs-4), were employed to regenerate aged base asphalt using first-principles calculations and molecular dynamics simulations. The optical properties of both the CQDs and the resulting CQDsRA, including band structure, electron density, molecular orbitals, and optical responses, were systematically examined. The results reveal that the type of CQDs significantly influences the optical response of CQDsRA. Moreover, the different CQDs also markedly affect the fundamental properties and regeneration efficacy of the modified asphalt. Among the four types, CQDs-4 exhibits the strongest fluorescence intensity, whereas CQDs-1 shows the weakest. The molecular trajectories of the CQDs resemble those of a standard pyrometric cone during the regeneration process. Additionally, the chemical reactions occur between the CQDs and the aged asphalt, leading to the formation of a cross-linked network structure.

1. Introduction

Maintenance and repair operations of asphalt pavements generate large volumes of reclaimed asphalt pavement (RAP) materials (Xiao et al., 2023; Li et al., 2024b). In alignment with the strategic goals of carbon peaking and carbon neutrality, recycling waste or aged asphalt mixtures, recognized as a form of solid waste valorization, has attracted widespread attention, with various typical techniques being actively explored (Chen et al., 2020). Waste asphalt is a specific type of aged asphalt (Jalilov et al., 2017; Schneider et al., 2023), and the effectiveness of its regeneration is directly linked to the performance of recycled asphalt mixtures (Xu et al., 2024; Yi et al., 2023).

By incorporating regenerator or fresh asphalt, the composition, structure, and rheological properties of aged asphalt can be partially restored toward their original state (Stokstad, 2020). However, regenerated aged asphalt exhibits greater compositional complexity than its aged counterpart, as it comprises not only the regenerator but also the residual aged binder. Among its properties, rheology is particularly critical for the practical application of regenerated asphalt.

Aged asphalt forms as a result of oxidative aging, which increases the concentration of asphaltenes (Humes et al., 2023; Niles et al., 2020). As the degree of aging intensifies, the contents of saturates and aromatics, components known for their fluorescence responsiveness, decrease. Consequently, the fluorescence intensity weakens, while the overall optical response becomes stronger (Glattke et al., 2022; Wang et al., 2022). This enhanced optical response significantly influences the surface temperature of recycled asphalt pavements, causing temperatures to rise to 70–80 °C during summer months. Elevated pavement temperatures not only exacerbate distresses such as rutting, shoving, and bleeding but also intensify the urban heat island effect (Wang

* Corresponding author.
E-mail address: zxx09432338@sxu.edu.cn (X.-X. Zhou).
Peer review under the responsibility of China University of Petroleum (Beijing).

https://doi.org/10.1016/j.petsci.2026.06.048

et al., 2023; Dai et al., 2024). Therefore, investigating the optical properties of regenerated aged asphalt is of great significance for mitigating pavement overheating and alleviating urban heat island effects.

Recent studies have shown that carbon quantum dots (CQDs) exhibit excellent optical responsiveness and strong fluorescence (Wu et al., 2025; Sarkar et al., 2026). Moreover, CQDs-modified asphalt demonstrates improved anti-aging performance and contributes to reducing the urban heat island effect (He et al., 2023). Structurally, CQDs are classified, based on their parent fluorescent frameworks, into graphene quantum dots, carbon nanodots, and polymer dots. With typical diameters ranging from 1 to 10 nm, CQDs can significantly enhance the fluorescence of aged asphalt, suppress its excessive optical absorption, and thereby facilitate both regeneration and performance enhancement (Guo et al., 2016; Zhang et al., 2024). Leveraging these optical attributes, carbon quantum dot-regenerated aged asphalt (CQDsRA) has been developed to enable high-efficiency regeneration of aged binders.

However, key challenges remain: the underlying regeneration mechanism of CQDsRA is not yet fully understood, and robust methods for evaluating its rheological and optical properties are still lacking, issues that currently hinder broader research and application.

Although numerous studies have employed molecular simulations to investigate aged asphalt regeneration (Li et al., 2024a; Tian et al., 2025), conventional experimental approaches often rely on trial-and-error methodologies, which are time-consuming and resource-intensive. Fortunately, substantial experimental and modeling data already exist for carbon-based materials (e.g., biochar, CQDs) and aged asphalt (Zhou et al., 2024; Guo et al., 2024). If the rheological and optical properties of CQDsRA could be accurately predicted through molecular simulation and subsequently validated with minimal experimental effort, significant time and cost savings would be achieved.

Research on CQDsRA remains in its early stages, and several critical issues must be addressed before engineering-scale implementation becomes feasible. To this end, a CQDsRA formulation featuring high solar reflectance (or low solar absorption), strong fluorescence intensity, and superior regeneration capability is being designed. Such a material aims to: reduce summer pavement temperatures of recycled asphalt mixtures, enhance pavement fluorescence for potential smart-road applications, promote efficient regeneration of aged asphalt and its mixtures, mitigate high-temperature-related distresses, and extend the service life of recycled asphalt pavements (Wang et al., 2019).

CQDs can be synthesized via co-pyrolysis of waste wood chips or waste rubber powder, or through oxidative dialysis using hydrogen peroxide, yielding nanomaterials characterized by low solar absorption and high fluorescence intensity. Nevertheless, the rheological and optical behaviors of CQDsRA remain poorly understood.

To address these gaps, this study employs CQDs as multifunctional agents: targeting volatile organic compounds (VOCs) in waste asphalt through adsorption and acting as fluorescent molecular probes to detect polycyclic aromatic hydrocarbons (PAHs). By elucidating this dual targeting mechanism, the work aims to achieve green, sustainable preparation and high-value utilization of CQDsRA. Both molecular simulations and experimental methods are integrated to investigate its rheological and optical properties. The findings are expected to minimize waste and environmental pollution associated with wood chips, rubber powder, and waste asphalt, offering significant contributions to advancing the “dual carbon” (carbon peaking and carbon neutrality) strategic goals in road engineering.

2. Materials and experiments section

2.1. Raw materials

Waste wood chips were sourced from the Jinzhong Wood Processing Plant (Shanxi Province, China). Waste rubber powder was provided by Changzhou Rong Ao Chemical New Materials Co., Ltd., with a particle size of 40 mesh. The 70# asphalt was supplied by Hubei Guochuang Hi-Tech Materials Co., Ltd. Acetic acid, hydrogen peroxide, sulfuric acid, and triethylamine were all of analytical purity.

2.2. The preparation of CQDs and CQDsRA

The optimal mass ratio of waste wood chips to waste rubber powder (without pretreatment) was 6:4 according to the previous research (Zhang et al., 2025). To synthesize CQDs-1, 10 g of waste wood chips and waste rubber powder were placed into a 150 mL Teflon-lined hydrothermal reactor. Subsequently, 4 mL of sulfuric acid (used as a catalyst) and 96 mL of deionized water were added to the liner. The mixture was then heated at 200 °C for 10 h. After the reaction, the resulting CQDs solution was centrifuged at 10,000 rpm for 30 min to remove large particles. The supernatant was dialyzed using a 1000 Da dialysis membrane (regenerated cellulose) for 24 h and changed the water every 6 h, and the dialysate was subsequently freeze-dried at −50 °C and 12 h to obtain CQDs-1 powder. The synthesis of CQDs-2 followed the same procedure as that of CQDs-1, except that 6 mL of acetic acid was used as the catalyst instead of sulfuric acid. For CQDs-3, the process was modified by adding 4 mL of acetic acid and 2 g of triethylamine as co-catalysts. In the case of CQDs-4, the raw material composition was adjusted to 6 g of waste wood chips and 4 g of waste rubber powder (maintaining the 6:4 mass ratio), while the rest of the procedure remained identical to that of CQDs-1. To prepare aged asphalt, 350 g of 70# asphalt was first heated at 135 °C for 5 h until fully molten. Then, the samples were put into the rotating film oven test (RTFOT) at 163 °C ± 0.5 °C and 85 min. Long-term aged asphalt (AA) was then produced using a pressure aging vessel (PAV) at 100 °C and 2.1 ± 0.1 MPa for the standard conditioning period according to ASTM D6521. Subsequently, the synthesized CQDs with 1% mass ratio were incorporated

Table 1
The fundamental properties of asphalt.

Material	Penetration (25 °C), ×0.1 mm	Softening point, °C	Ductility (15 °C), cm
Asphalt	64	49	134
AA	48	65	105
CQDsRA-1	63	49	>150
CQDsRA-2	61	50	>150
CQDsRA-3	59	51	>150
CQDsRA-4	56	52	>150

Table 2
The four components of asphalt.

Material	Asphaltenes, %	Saturates, %	Aromatics, %	Resins, %
Asphalt	16.1 ± 0.2	12.5 ± 0.2	23.5 ± 0.5	47.9 ± 0.5
AA	28.5 ± 0.5	11.5 ± 0.2	15.1 ± 0.2	44.9 ± 0.5
CQDsRA-1	17.1 ± 0.2	13.7 ± 0.2	37.2 ± 0.5	32.0 ± 0.5
CQDsRA-2	18.9 ± 0.2	14.1 ± 0.2	38.3 ± 0.5	28.7 ± 0.5
CQDsRA-3	23.7 ± 0.5	15.2 ± 0.2	26.4 ± 0.5	34.7 ± 0.5
CQDsRA-4	24.3 ± 0.5	14.5 ± 0.2	28.6 ± 0.5	32.6 ± 0.5

into the aged asphalt and mixed under high-speed shear at 2000 rpm for 1 h to produce carbon quantum dot-regenerated aged asphalt (CQDsRA). The fundamental properties of the CQDsRA are summarized in Table 1. Penetration, softening point, and ductility were measured in accordance with ASTM D5, ASTM D36, and ASTM D113, respectively.

Penetration reflects the hardness of asphalt, while the softening point and ductility are physical indicators of its high-temperature and low-temperature performance, respectively. As shown in Table 1, the penetration of CQDsRA is lower than that of virgin (base) asphalt but higher than that of long-term aged asphalt (AA), indicating that the addition of carbon quantum dots (CQDs) effectively softens the aged binder, restoring its penetration close to that of the original base asphalt. Among the four

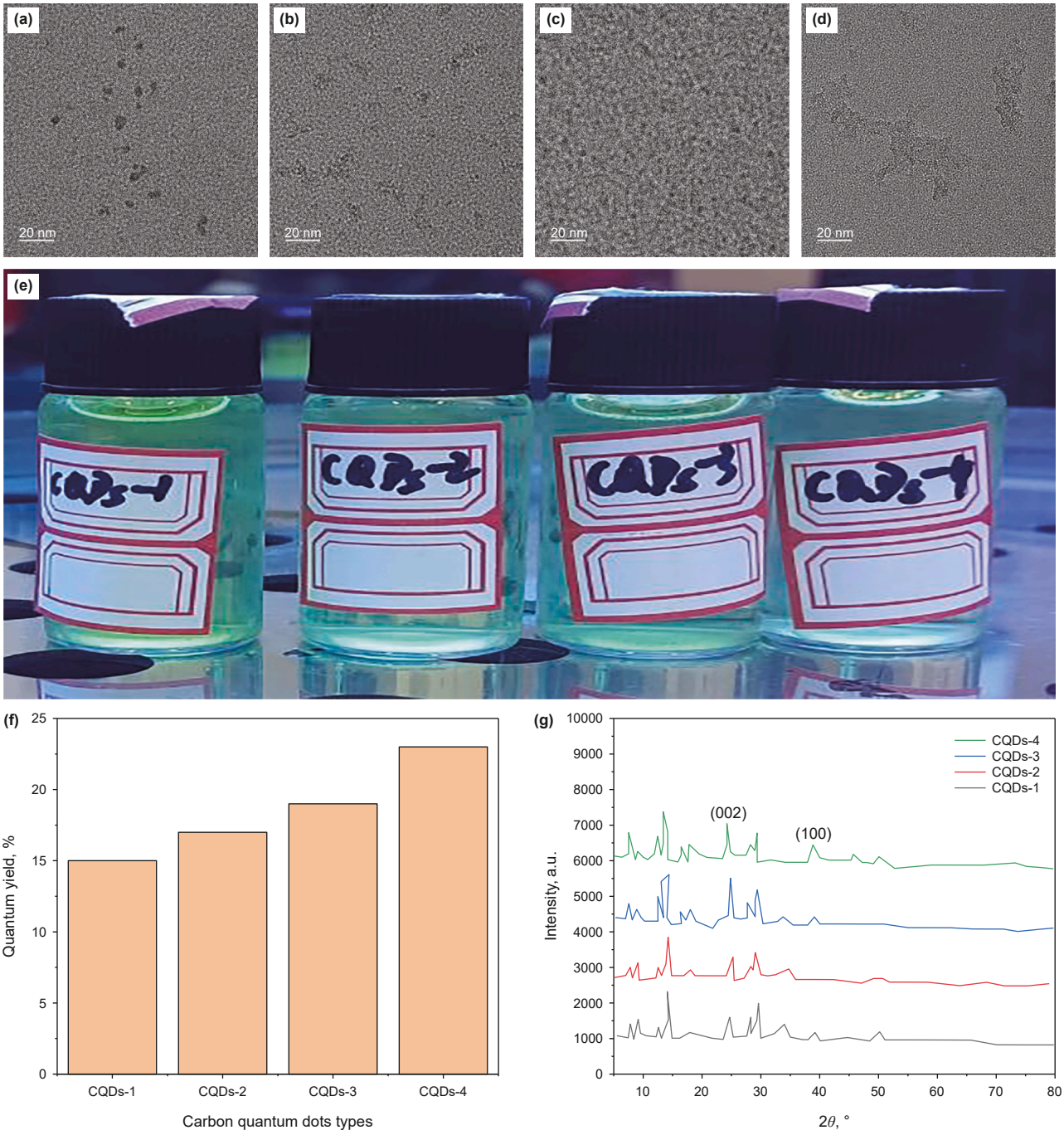

Fig. 1. TEM morphology, photos under UV light irradiation, quantum yield, and X-ray diffraction (XRD) pattern of CQDs: **(a)** CQDs-1, **(b)** CQDs-2, **(c)** CQDs-3, **(d)** CQDs-4, **(e)** photos of CQDs, **(f)** quantum yield, **(g)** XRD.

types, CQDs-1 exhibits the strongest softening effect, greater than that of CQDs-2, CQDs-3, and CQDs-4, while CQDs-4 shows the weakest regeneration performance.

The softening point and ductility results further reveal that the incorporation of CQDs reduces the high-temperature stability (as indicated by a lower softening point) but improves the low-temperature flexibility (as evidenced by increased ductility). These findings collectively demonstrate that CQDs possess a clear regenerative capability for aged asphalt.

The four-component fractions (saturates, aromatics, resins, and asphaltenes) of both long-term aged asphalt and CQDsRA were analyzed according to the Chinese industrial standard NB/SH/T 0509–2010. As shown in Table 2, compared to base asphalt, the chemical equilibrium of aged asphalt (AA) is disrupted: the contents of light components, saturates and aromatics, decrease significantly, while the asphaltenes content increases, rendering the binder harder and more brittle. The standard deviation of CQDsRA is less than that of 0.5. In contrast, the addition of CQDs reverses this aging-induced trend. Specifically, CQDs-1, CQDs-2, CQDs-3, and CQDs-4 all promote a gradual shift in the four-component composition back toward that of the base asphalt. This confirms that CQDs exhibit a pronounced regenerative effect on long-term aged asphalt.

The transmission electron microscope (TEM) morphology of CQDs showed in Fig. 1. The average size of CQDs-1, CQDs-2, CQDs-3, and CQDs-4 is 3.8 nm, 3.2 nm, 2.5 nm, and 2.8 nm, respectively. The CQDs appear pale yellow under UV light irradiation. The particle size was used to confirm that it was a CQDs.

Use 54% sulfuric quinine (denoted as QY) as the reference, calculate the QY of CDs according to Eq. (1).

$$Q_x = Q_R\left(\frac{I_x}{I_R}\right)\left(\frac{\eta_x^2}{\eta_R^2}\right)\left(\frac{A_R}{A_x}\right) \quad (1)$$

"Q" and "I" represent the fluorescence quantum yield and fluorescence intensity respectively in the formula. The parameter "η" indicates the refractive index of the solution; "A" represents the absorbance of the solution. The absorbance of the sample and quinine sulfate should be adjusted to below 0.1. The subscripts "x" and "R" respectively refer to the sample and the reference substance.

The quantum yield of CQDs is above 17% and the quantum yield of CQDs-4 is the biggest (22.8%), while the quantum yield of CQDs-1 is the smallest (17.5%). The CQDs types affected significantly the quantum yield of CQDs. The XRD pattern showed that the crystallinity of CQDs changed obviously with the change of CQDs types. The two characteristic peaks crystallinity of CQDs appeared at 25° and 40° increased with the change of CQDs types (from CQDs-1 to CQDs-4). It indicated that CQDs type would affect significantly the crystallinity.

2.3. Molecular models building

As shown in Fig. 2(a)–(d), the four carbon quantum dots (CQDs) were represented by their respective molecular formulas: $C_{34}H_{14}O_2$ as CQDs-1, $C_{52}H_{72}O_{14}$ as CQDs-2, $C_{39}H_{30}N_6O_{10}$ as CQDs-3, and $C_{52}H_{72}O_{10}S_4$ as CQDs-4. The amorphous cell module was used to construct the CQDs models, employing the COMPASS force field, fine quality settings, and a target density of 1.0 g/cm^3. The calculated diameters of CQDs-1, CQDs-2, CQDs-3, and CQDs-4 are 11.52, 11.78, 9.08, and 10.72 Å, respectively. The primary compositional difference between CQDs-1 and CQDs-2 lies in their oxygen content. The primary compositional difference between CQDs-2 and CQDs-3 is the nitrogen content. The primary compositional difference between CQDs-3 and CQDs-4 is the sulfur content.

As shown in Fig. 2(e)–(h), the base asphalt was modeled using the four-component asphalt system. Rubber was represented by the molecule $C_{12}H_{56}O_2S$. After aging, the molecular structure of the asphalt underwent significant changes, most notably an increase in oxygen content. The detailed molecular representations of the aged components are as follows: aged asphaltenes ($C_{42}H_{47}O_5$ $C_{51}H_{54}O_5S$ and $C_{66}H_{67}NO_7$), aged saturates ($C_{30}H_{62}$ and $C_{35}H_{62}$), aged aromatics ($C_{35}H_{36}O_4$ and $C_{30}H_{42}O_2$), aged resins ($C_{40}H_{55}NO_2$, $C_{40}H_{56}O_3S$, $C_{18}H_{10}O_3S_2$, $C_{36}H_{53}NO_2$, and $C_{29}H_{48}O_2$). These assignments are based on prior studies (Luo et al., 2024; Yu et al., 2024).

To investigate interactions between CQDs and the aged asphalt components, molecular models were constructed using the Amorphous Cell (AC) module with a 1% mass ratio of CQDs to each asphalt component (Ren et al., 2024). A CQDs loading of 1% mass ratio corresponds to one CQD molecule in the simulation system.

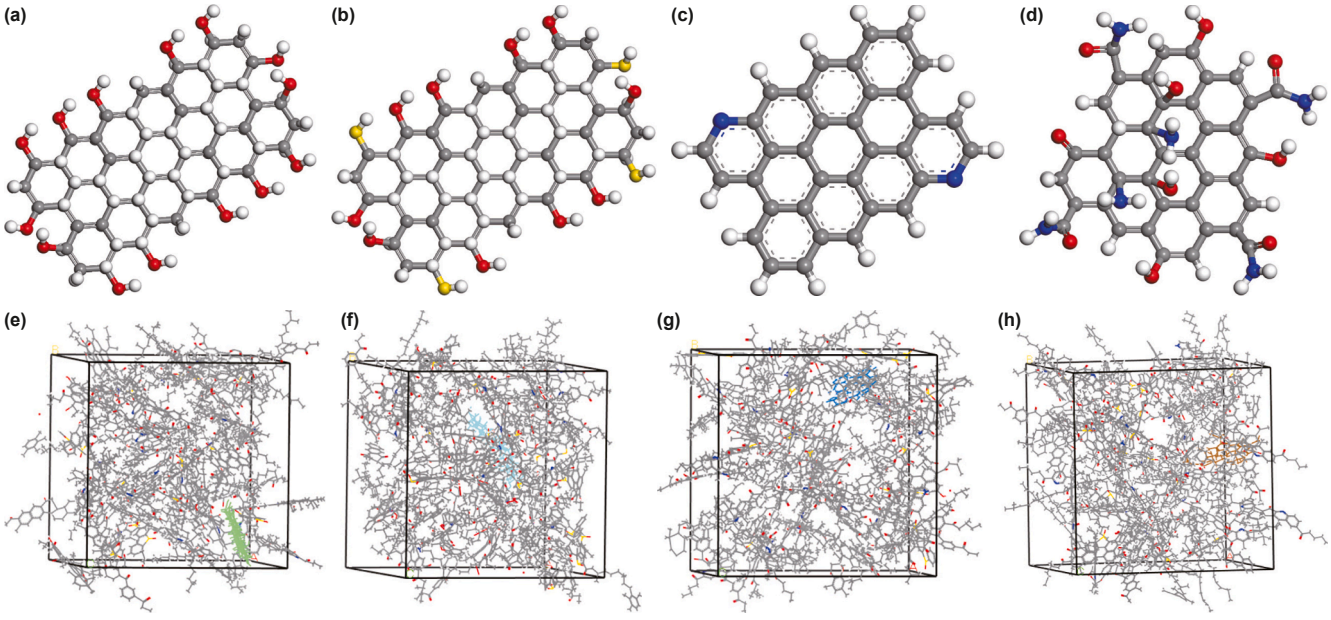

Fig. 2. The molecular models of CQDs and CQDsRA: **(a)** CQDs-1, **(b)** CQDs-2, **(c)** CQDs-3, **(d)** CQDs-4, **(e)** CQDsRA-1, **(f)** CQDsRA-2, **(g)** CQDsRA-3, **(h)** CQDsRA-4.

2.4. Molecular simulations of CQDsRA using first-principle

The CASTEP module was used to optimize the geometric structures and validate the accuracy of the molecular models. Geometry optimization was performed using the Broyden-Fletcher-Goldfarb-Shanno (BFGS) algorithm to adjust atomic positions and achieve energy minimization.

Subsequently, the optical properties of the carbon quantum dots (CQDs) and CQDs-regenerated aged asphalt (CQDsRA) were investigated using the Generalized Gradient Approximation (GGA) with the Perdew-Burke-Ernzerhof (PBE) functional. A $1 \times 1 \times 1$ Monkhorst-Pack k-point grid was employed for Brillouin zone sampling, and the plane-wave energy cutoff was set to 350 eV.

2.5. Molecular simulations of CQDsRA using molecular dynamic simulation

Amorphous module was used to build the CQDsRA with different CQDs contents and CQDs types. Then, Forcite module was used to conduct geometry optimization and molecular dynamic simulation. The geometry optimization parameters included Conjugate gradient algorithm, Fine convergence tolerance quality, and 1000 max iterations. The molecular dynamic simulation steps: NPT ensemble was used at the temperature of 298.15 K, the simulation step used 1 fs, the cutoff radius selected 16 Å, the simulation time was 100 ps with Nose thermostat and Andersen barostat. The density, glass transition temperature, and solubility parameter of CQDsRA were calculated.

3. Results and discussion

3.1. Optical properties of carbon quantum dots

As shown in Fig. 3(a), the UV-vis absorption spectra show CQDsRA absorption peaks at 225 nm (RA-1), 232 nm (RA-2), 251 nm (RA-3), and 245 nm (RA-4), with absorbance decreasing at shorter wavelengths. Compared to pristine CQDs, CQDsRA peaks are red-shifted, indicating altered electronic structure from asphalt interaction. As shown in Fig. 3(b), the reflectance spectra of CQDs increase with wavelength, peaking near 2050 nm, following the order RA-4 > RA-3 > RA-2 > RA-1, inversely correlating with CQDs molecular weight. S/N doping enhances reflectivity. As shown in Fig. 3(c), show single "pseudo-M″ emission peaks at 548, 532, 525, and 500 nm for RA-1 to RA-4, with intensities of ~320, 380, 1100, and 3500 a.u., respectively. Emission blue-shifts and intensity increases dramatically from RA-1 to RA-4. Both emission wavelength and intensity depend strongly on CQDs type, with fluorescence intensity increasing as O, N, S content decreases, likely due to non-radiative recombination pathways introduced by heteroatom doping. Overall, CQDsRA optical properties are highly tunable via compositional control, while asphaltenes polar/electronegative groups act as quenchers, suppressing fluorescence through collisional non-radiative energy dissipation.

To elucidate the electronic properties of carbon quantum dots (CQDs), the band structures and density of states (DOS) of the four CQDs types were investigated using first-principles calculations based on density functional theory (DFT). As shown in Fig. 4, The band gap of CQDs-1 is similar to CQDs-2, while CQDs-3 closely resembles CQDs-4, with CQDs-1's band gap lying between those of CQDs-2 and CQDs-3, demonstrating tunable electronic properties via compositional variation. S and N incorporation noticeably increases the band gap and alters band structure, whereas O content exerts only minor influence. These computational results agree well with the spectral data.

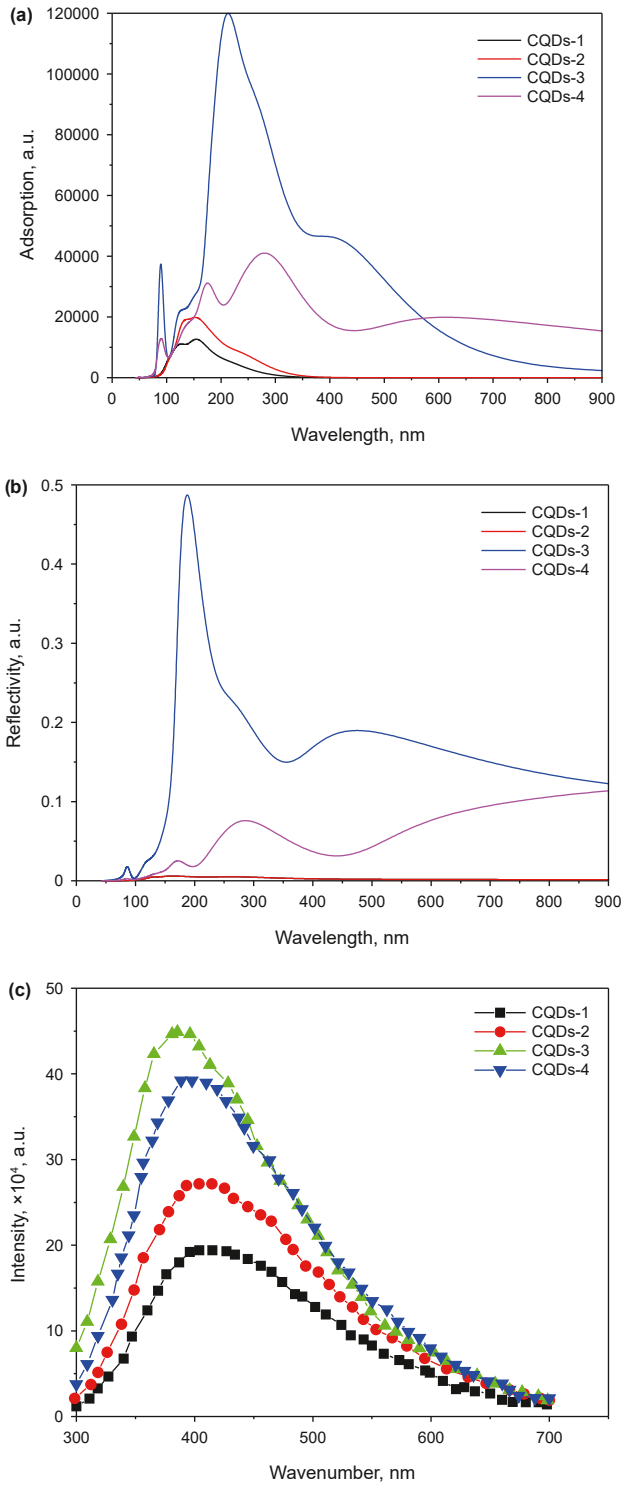

Fig. 3. The optical response spectrum of CQDs: **(a)** the absorption spectrum of CQDs, **(b)** the reflectance spectrum of CQDs, **(c)** the fluorescence spectrum of CQDs.

As shown in Fig. 5, yellow and blue isosurfaces indicate high electron density at reactive sites; more surrounded carbon atoms imply stronger electrophilic reactivity. LUMO reactive sites localize mainly around oxygen atoms. Electrophilic reactivity increases with CQDs molecular weight, suggesting strengthened quantum confinement effects with larger size and compositional variation. HOMO/LUMO distributions show spatial and electronic variability

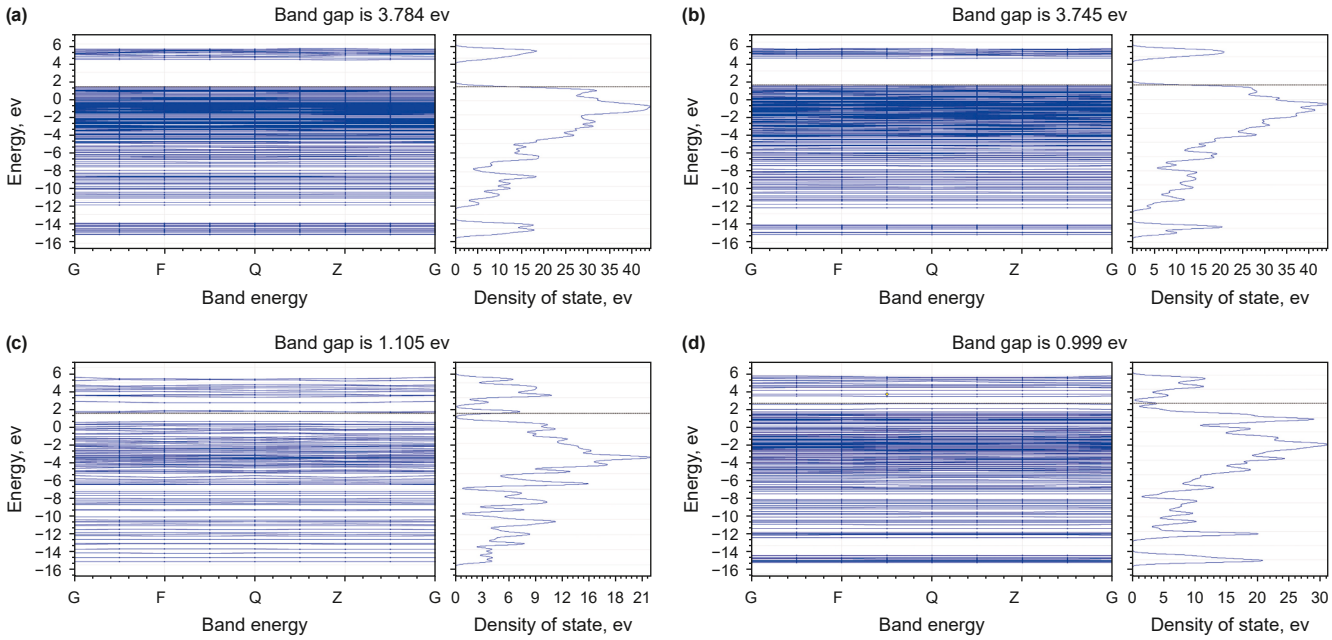

Fig. 4. The band structure of CQDs: **(a)** CQDs-1, **(b)** CQDs-2, **(c)** CQDs-3, **(d)** CQDs-4.

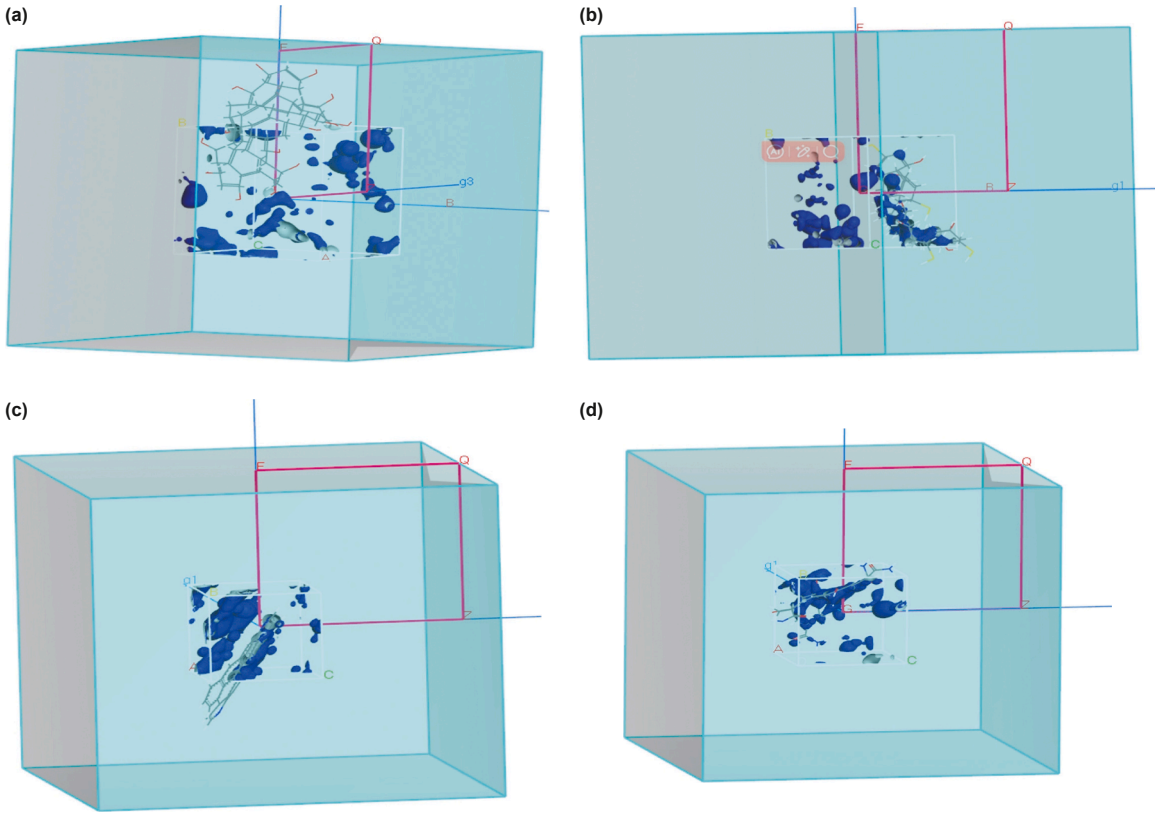

Fig. 5. The HOMO and LUMO distribution of CQDs with different types: **(a)** CQDs-1, **(b)** CQDs-2, **(c)** CQDs-3, **(d)** CQDs-4.

depending on CQDs type, reflecting differences in local chemical environment and electronic structure.

The electron density distributions of the carbon quantum dots (CQDs) are shown in Fig. 6. The electron density of CQDs-1 is higher than that of CQDs-2, CQDs-3, and CQDs-4. CQDs-4 exhibits higher electron density than both CQDs-2 and CQDs-3. CQDs-2 shows higher electron density than CQDs-3. These results indicate that the electron-donating (or electron-attracting) capability, referred to here as electron density strength, follows the order: CQDs-1 > CQDs-4 > CQDs-2 > CQDs-3, with CQDs-1 possessing the strongest

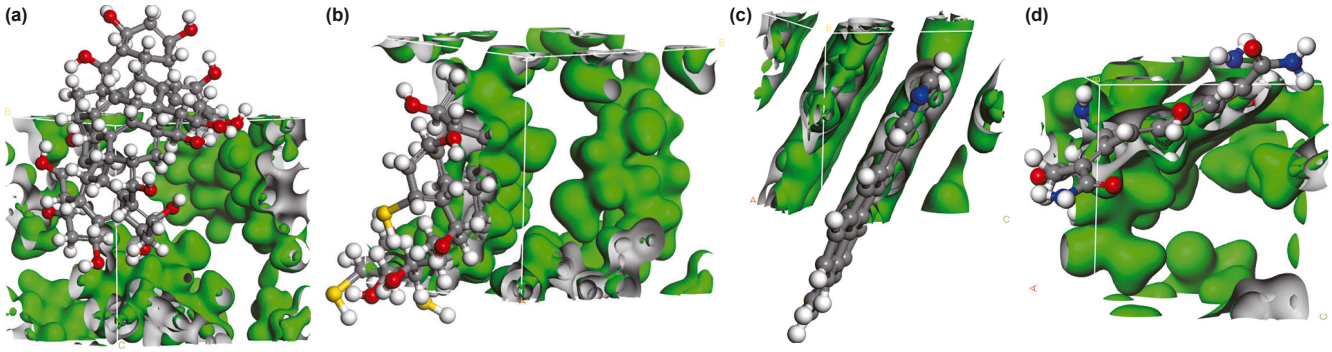

Fig. 6. The electron density of CQDs: **(a)** CQDs-1, **(b)** CQDs-2, **(c)** CQDs-3, **(d)** CQDs-4.

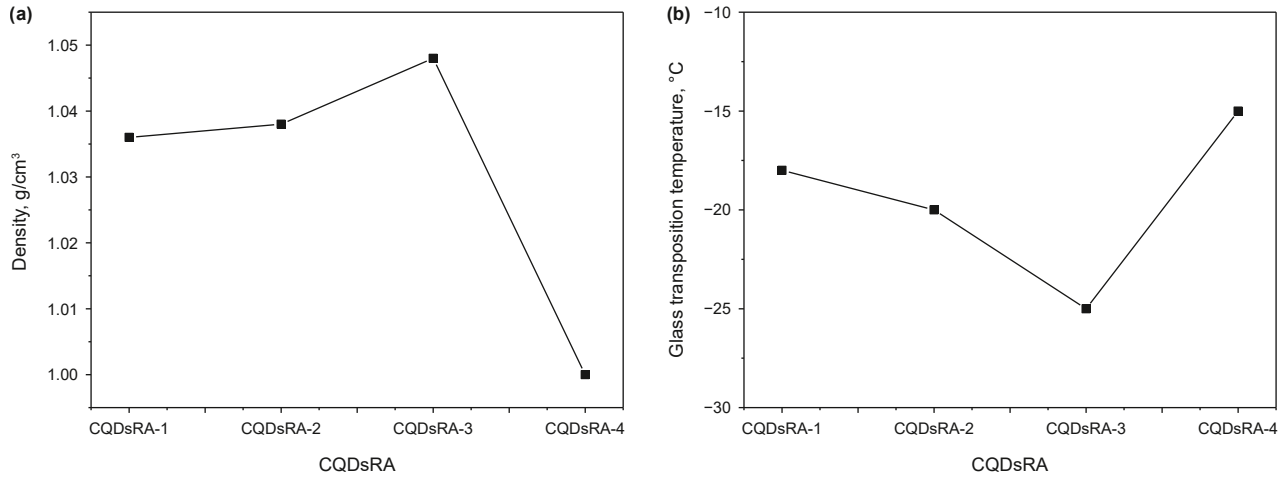

Fig. 7. The density and glass transposition temperature of CQDsRA: **(a)** density, **(b)** glass transposition temperature.

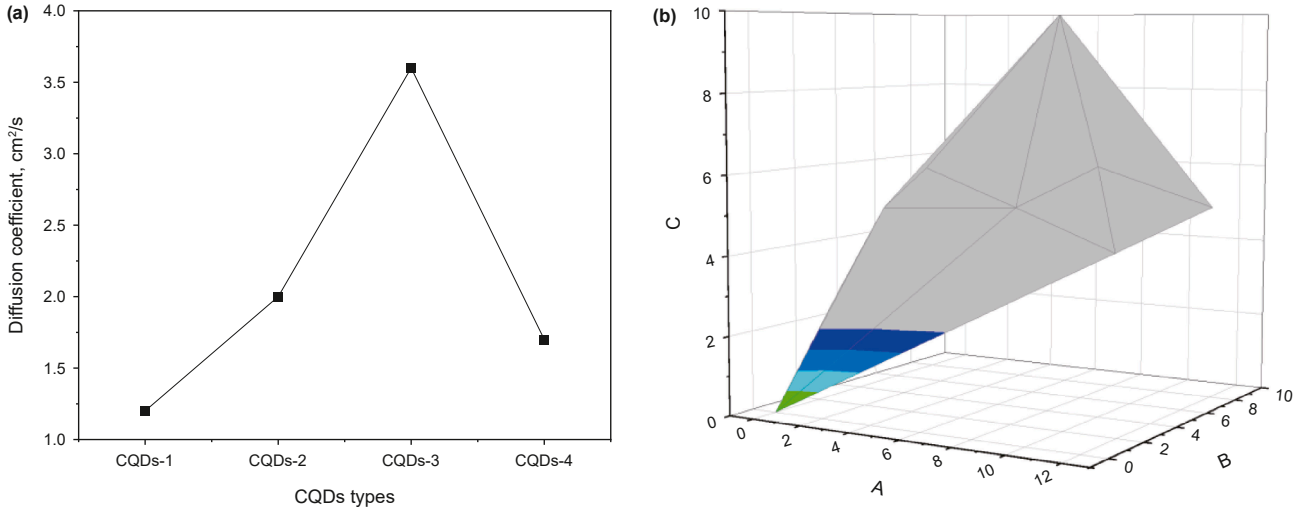

Fig. 8. The molecular movement of CQDsRA: **(a)** diffusion coefficient, **(b)** molecular movement trajectory curves.

electron density and CQDs-3 the weakest. When correlated with the molecular structures of the CQDs, it becomes evident that an increase in oxygen (O) and nitrogen (N) content tends to reduce the electron density strength, whereas a higher sulfur (S) content enhances it. This suggests that heteroatom doping significantly modulates the electronic properties of CQDs, with S acting as an electron-density promoter and O/N acting as suppressors.

3.2. Molecular simulations of carbon quantum dots regenerated aged asphalt

3.2.1. The fundamental properties of CQDsRA with molecular simulations

As shown in Fig. 7(a), the simulated density decreases with temperature, following CQDsRA-1 < CQDsRA-2 < CQDsRA-

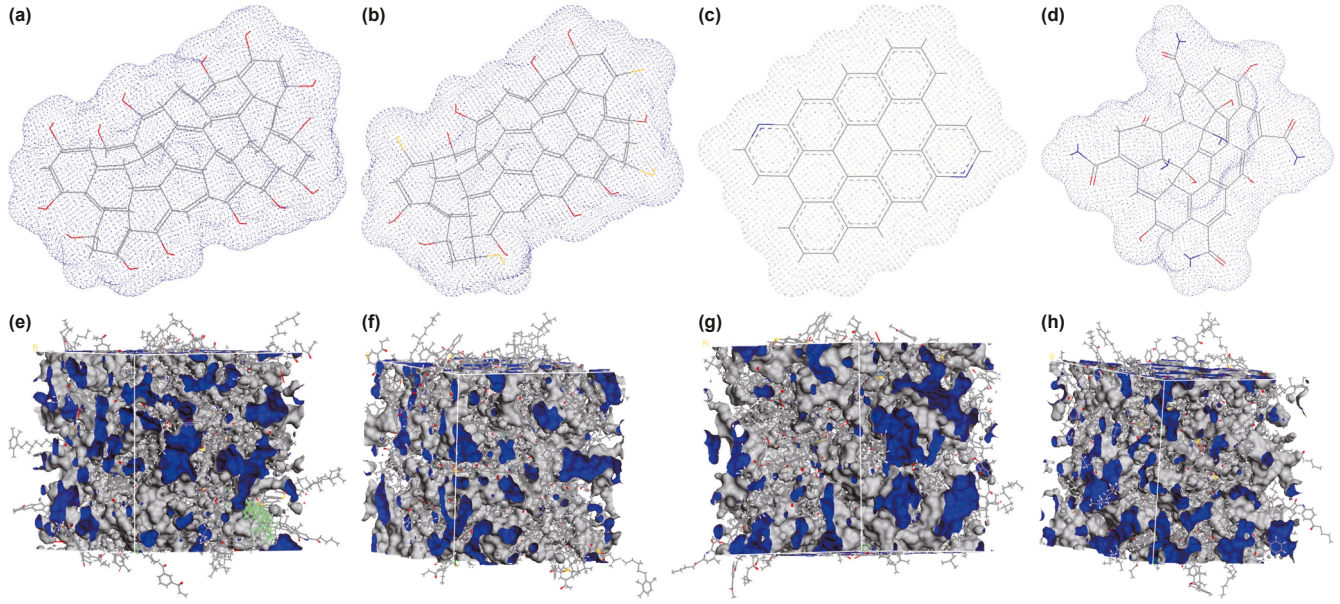

Fig. 9. The free volume of CQDs and CQDsRA system: **(a)** CQDs-1, **(b)** CQDs-2, **(c)** CQDs-3, **(d)** CQDs-4, **(e)** CQDsRA-1, **(f)** CQDsRA-2, **(g)** CQDsRA-3, **(h)** CQDsRA-4.

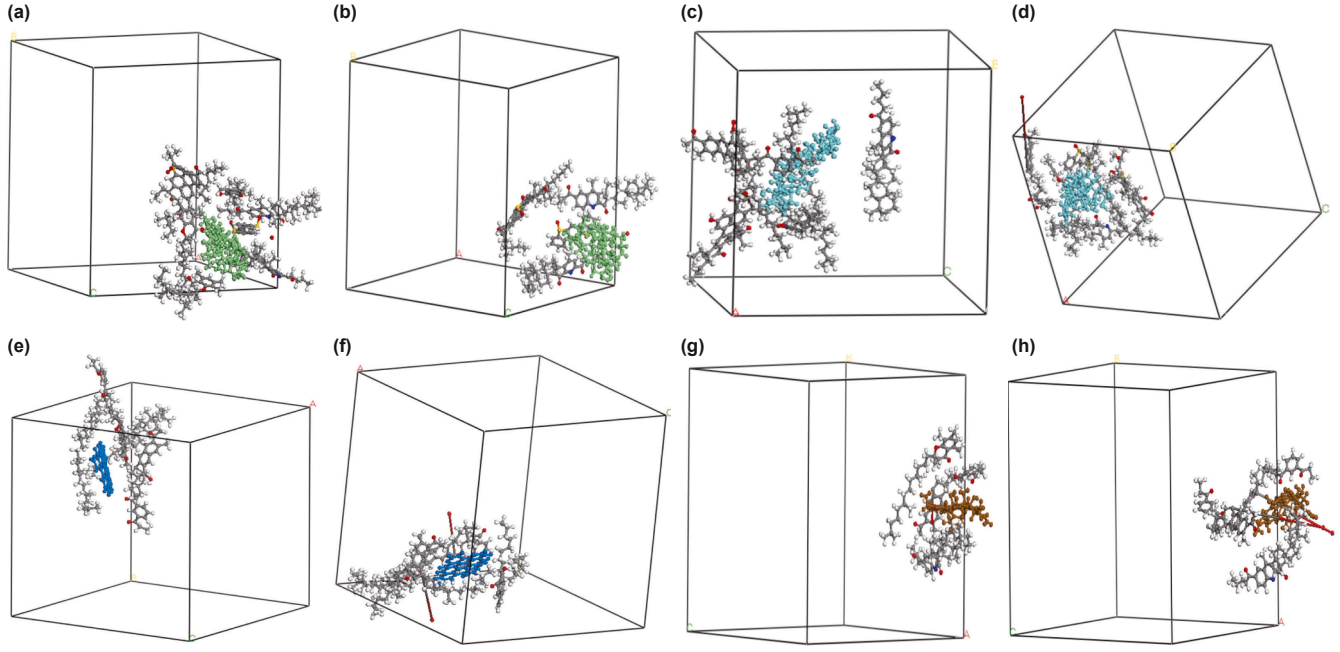

Fig. 10. The arrangement modes between CQDs and adjacent molecules during the molecular movement process: **(a)** the initial position between CQDs-1 and the adjacent molecules, **(b)** the final position between CQDs-1 and the adjacent molecules, **(c)** the initial position between CQDs-2 and the adjacent molecules, **(d)** the final position between CQDs-2 and the adjacent molecules, **(e)** the initial position between CQDs-3 and the adjacent molecules, **(f)** the final position between CQDs-3 and the adjacent molecules, **(g)** the initial position between CQDs-4 and the adjacent molecules, **(h)** the final position between CQDs-4 and the adjacent molecules.

4 < CQDsRA-3. Experimental results agree within 10% deviation. CQDsRA-1, -2, and -3 have densities (~1.04 g/cm^3) close to base asphalt (1.00 g/cm^3), suggesting better compatibility than CQDsRA-4. As shown in Fig. 7(b), the Simulated Tg values range from −30 to 0 °C, following CQDsRA-4 > CQDsRA-1 > CQDsRA-2 > CQDsRA-3, indicating that CQDs chemical composition, particularly heteroatom (O, N, S) content, strongly influences glass transition behavior by affecting chain mobility and intermolecular interactions.

3.2.2. Diffusion coefficients of CQDsRA with molecular simulations

As shown in Fig. 8(a), the diffusion coefficients (D) of CQDsRA initially increase with changes in CQDs type and then decrease. Specifically, the diffusion coefficient follows the order: CQDsRA-1 < CQDsRA-2 < CQDsRA-4 < CQDsRA-3, with CQDsRA-1 exhibiting the lowest D and CQDsRA-3 the highest. These results clearly demonstrate that the type of CQDs significantly influences the diffusion behavior of CQDsRA, highlighting the role of CQDs composition in modulating molecular mobility within the asphalt matrix.

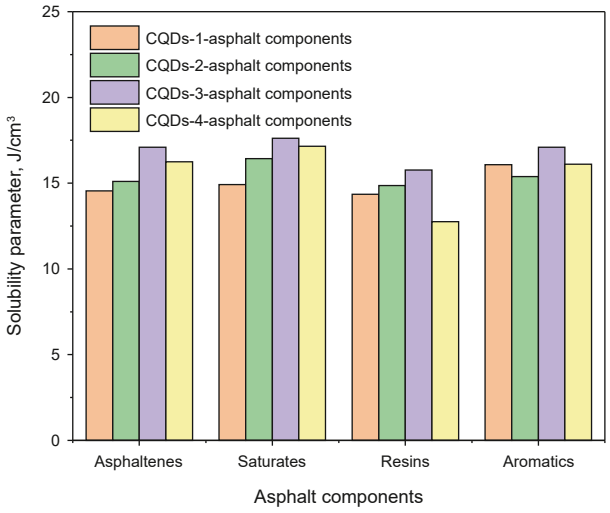

Fig. 11. The solubility parameter of CQDsRA system.

3.2.3. Molecular movement of CQDsRA with molecular simulations

Molecular trajectory analysis was employed to evaluate the molecular mobility of carbon quantum dot-regenerated aged asphalt (CQDsRA). The molecular movement trajectories of CQDsRA are presented in Fig. 8(b). Within the regenerated asphalt matrix, the motion of CQDs appears initially chaotic. However, when aged saturates and aromatics are highlighted in distinct colors, it becomes evident that CQDs consistently migrate toward these lighter fractions, specifically, aged saturates and aromatics. In contrast, aged asphaltenes tend to move away from one another in the presence of CQDs. Additionally, only a few small molecules escape the simulation box, indicating good system stability.

The overall trajectory of CQDs resembles a standard pyrometric cone: molecules depart from their initial positions, travel outward, and then return toward their starting locations, suggesting localized yet dynamic motion with partial reversibility. Molecular mobility can also be assessed through occupied volume: a smaller occupied volume generally corresponds to greater molecular mobility (i.e., faster movement). As shown in Fig. 9, the occupied volumes of CQDs-1, CQDs-2, CQDs-3, and CQDs-4 are 868.55, 906.45, 411.64, and 611.02 Å^3, respectively. Among them, CQDs-2 has the largest occupied volume, while CQDs-3 has the smallest, indicating that CQDs-3 exhibits the highest molecular mobility. These results confirm that the chemical structure and composition of CQDs significantly influence their molecular dynamics.

Excess molecules were removed from the CQDsRA systems, retaining only the carbon quantum dots (CQDs) and their adjacent molecules before and after molecular movement. As shown in Fig. 10, the number and average distance of surrounding molecules decrease after movement, indicating selective expulsion of incompatible molecules and attraction of compatible ones, optimizing local interactions. Among the four types, positional change follows CQDs-3 > CQDs-2 > CQDs-4 > CQDs-1. Arrangement patterns differ markedly before and after movement, with distinct optimal configurations across CQDsRA systems. These results confirm highly selective, system-specific reorganization at the CQDs–asphalt interface, with adjacent molecule composition and distribution varying significantly by CQDs type.

3.2.4. Molecular compatibility of CQDsRA with molecular simulations

The solubility parameter was used to assess the molecular compatibility between carbon quantum dots (CQDs) and the components of regenerated aged asphalt (CQDsRA). As shown in Fig. 11, the smallest solubility parameter difference occurs with aged saturates and the largest with aged asphaltenes, indicating CQDs are most compatible with saturates and least with asphaltenes. Among the four CQDs types, the parameter difference follows CQDs-1 < CQDs-2 < CQDs-3 < CQDs-4, yielding a compatibility order of CQDs-1 > CQDs-2 > CQDs-3 > CQDs-4. These results confirm that CQDs chemical structure significantly governs molecular compatibility, dispersion stability, and interfacial interactions in CQDsRA systems.

3.2.5. Rheological properties of CQDsRA

The rheological properties of CQDsRA are presented in Fig. 12. It shows G^* decreasing and δ increasing with temperature, consistent with typical asphalt viscoelasticity. Stiffness follows CQDsRA-1 > CQDsRA-2 > CQDsRA-3 > CQDsRA-4, while phase angle shows the opposite trend, indicating CQDsRA-1 is most elastic and CQDsRA-4 most viscous. No abrupt changes in G^* or δ confirm good CQDs–asphalt compatibility and absence of phase separation. The higher G^* of CQDsRA-1 suggests strengthened intermolecular interactions, promoting asphalt regeneration. The rutting factor G^*/

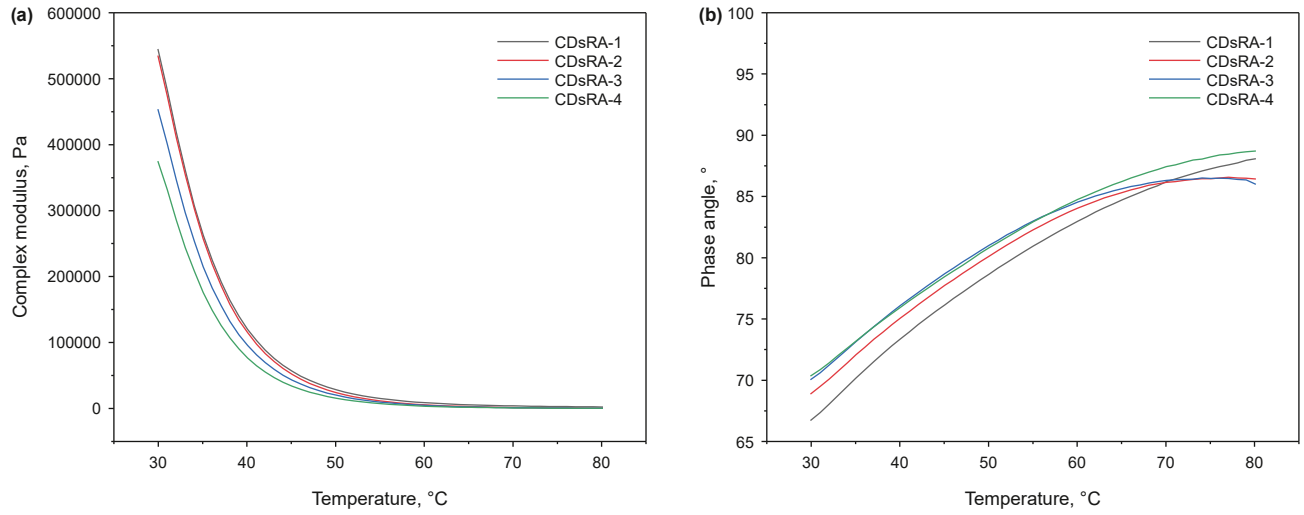

Fig. 12. The temperature scanning curves of CQDsRA: **(a)** complex modulus, **(b)** phase angle.

sinδ decreases with temperature due to enhanced molecular thermal motion, indicating reduced high-temperature deformation resistance at elevated temperatures.

3.3. Optical properties of CQDsRA

As shown in Fig. 13(a), the UV-vis absorption spectra of CQDsRA exhibit distinct characteristic peaks: CQDsRA-1 at 225 nm, CQDsRA-2 at 232 nm, CQDsRA-3 at 251 nm, CQDsRA-4 at 245 nm. Overall, the absorbance of CQDsRA decreases with decreasing wavelength. These results indicate that the type of CQDs significantly influences both the position of the absorption peaks and the overall absorbance intensity. Compared to the absorption spectra of pristine CQDs, the absorption peaks of CQDsRA are red-shifted, it shifted toward longer wavelengths, suggesting that interaction with aged asphalt alters the electronic structure and optical properties of the CQDs.

As shown in Fig. 13(b), the reflectance spectra of CQDsRA show an overall increasing trend with wavelength, reaching a maximum around 2050 nm. The reflectivity follows the order: CQDsRA-4 > CQDsRA-3 > CQDsRA-2 > CQDsRA-1, indicating that CQDsRA-4 exhibits the highest reflectivity, while CQDsRA-1 shows the lowest. This trend correlates with molecular weight: reflectivity decreases as the molecular weight of the CQDs increases. However, for a given sample, reflectivity increases with decreasing wavelengths across the measured range. Furthermore, the incorporation of hetero-atoms such as sulfur (S) or nitrogen (N) enhances the reflectivity of CQDsRA, suggesting that S/N doping plays a positive role in modulating its optical response.

As shown in Fig. 13(c), the fluorescence spectra show single "pseudo-M" emission peaks at 548, 532, 525, and 500 nm for CQDsRA-1 to RA-4, with intensities of ~320, 380, 1100, and 3500 a.u., respectively. Emission blue-shifts and intensity increases dramatically from RA-1 to RA-4. Both wavelength and intensity depend strongly on CQDs type, with intensity increasing as O, N, S content decreases, likely due to non-radiative recombination pathways from heteroatom doping. Thus, CQDsRA optical behavior is tunable via compositional control, with higher heteroatom content yielding stronger, bluer emission. Fluorescence quenching occurs via collisional energy transfer to polar/electronegative groups (e.g., S, O-containing species) in asphalt, dissipating excitation energy non-radiatively.

As shown in Fig. 14(a) and (b), Raman spectra of CQDs-1 to CQDs-4 show characteristic D (~1328 cm^{-1}) and G (~1572 cm^{-1}) bands with identical I_D/I_G ratios of 1.2, indicating negligible graphitic structure changes from amino-hydrothermal treatment, while the high ratio suggests small crystallite sizes from acid exfoliation. CQDsRA composites exhibit additional peaks at 3065 (aromatic C–H), 2906 (aliphatic C–H), 1966 (acetylene-like C_2H_2), and 1386 cm^{-1} (CO_2/carbonate), with distinct intensity variations among samples reflecting different molecular interactions.

As shown in Fig. 14(c) and (d), FT-IR spectra reveal bands at 2921/2849 cm^{-1} (–CH_2–), 1760 cm^{-1} (C=O/S=O), and 1456 cm^{-1} (N–H/CH deformation). Notably, the 1760 cm^{-1} peak absent in aged asphalt appears in all CQDsRA, originating from CQDs surface functionalities. Spectral shifts confirm chemical interactions between CQDs and aged asphalt, forming a cross-linked network that enhances compatibility. Reduced intermolecular spacing promotes PAH aggregate formation via π-π stacking, altering electronic structure and causing fluorescence quenching.

As shown in Fig. 15, the fluorescence Micro-graph reveal distinct morphological and optical differences between CQDs and CQDsRA. The pristine CQDs exhibit particle-like morphology, whereas CQDsRA displays sheet-like structures, indicating strong interaction between the CQDs and the aged asphalt matrix. Moreover, CQDs-1, CQDs-2, CQDs-3, and CQDs-4 emit different

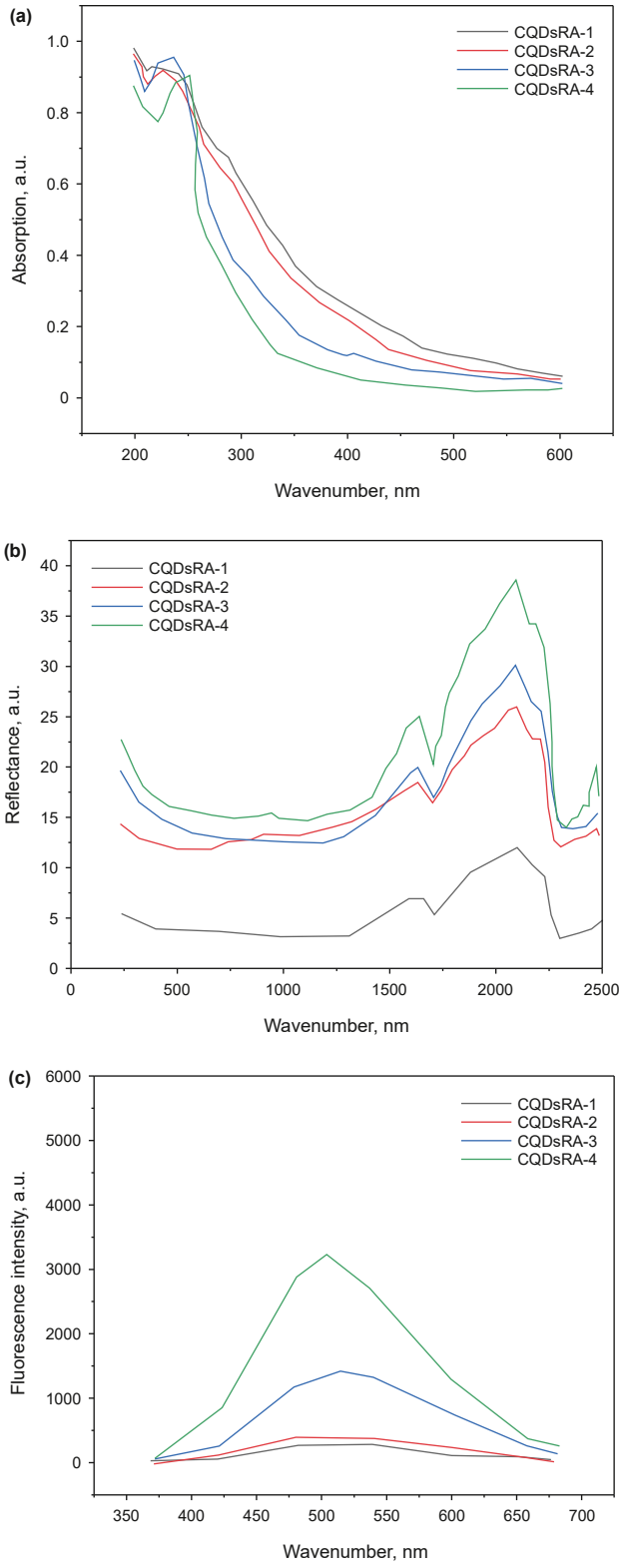

Fig. 13. The optical response of CQDsRA: **(a)** the absorption spectrum of CQDsRA, **(b)** the reflectance spectrum of CQDsRA, **(c)** the fluorescence spectrum of CQDsRA.

fluorescence colors, reflecting variations in their surface chemistry and electronic structure. Typically, regenerated asphalt (RA) or conventional asphalt does not exhibit noticeable fluorescence under the same conditions. In contrast, all CQDsRA samples show clear fluorescence, which is attributed to the introduction of CQDs

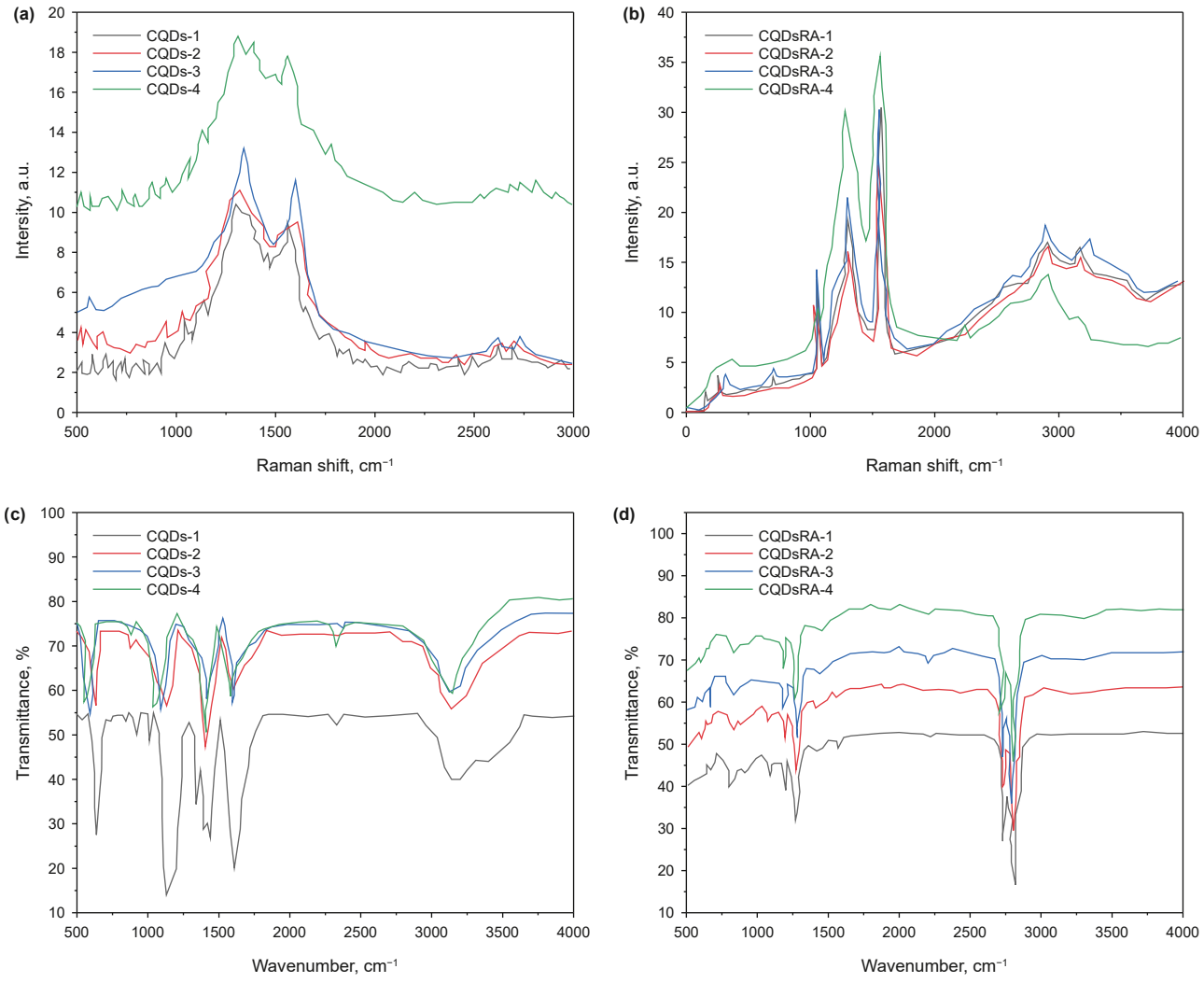

Fig. 14. The Raman spectra and FT-IR of CQDs/CQDsRA: **(a)** Raman spectra of CQDs, **(b)** Raman spectra of CQDsRA, **(c)** FT-IR of CQDs, **(d)** FT-IR of CQDsRA.

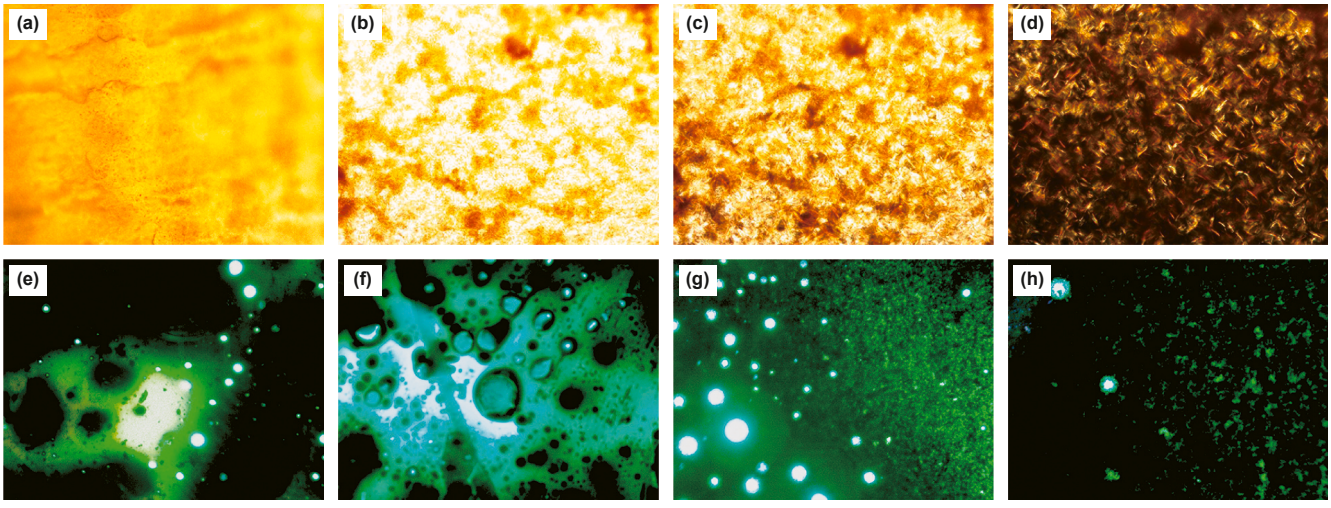

Fig. 15. The fluorescence micro-morphology of CQDs and CQDsRA: **(a)** CQDs-1, **(b)** CQDs-2, **(c)** CQDs-3, **(d)** CQDs-4, **(e)** CQDsRA-1, **(f)** CQDsRA-2, **(g)** CQDsRA-3, **(h)** CQDsRA-4.

that significantly enhance the fluorescence intensity of the composite system. Previous studies have reported that polycyclic aromatic hydrocarbons (PAHs), common components in asphalt, can exhibit fluorescence. However, this effect is often too weak to be observed in bulk asphalt, likely due to fluorescence quenching caused by other asphalt constituents (e.g., asphaltenes, metals, or hetero-atoms) that suppress radioactive recombination. Thus, the absence of detectable fluorescence in neat asphalt is probably due to both the inherently low quantum yield of PAHs and the quenching effects of the complex asphalt matrix. The strong and tunable fluorescence observed in CQDsRA therefore originates primarily from the CQDs themselves, not from native asphalt components, highlighting their role as effective fluorescent probes and functional modifiers in asphalt regeneration.

4. Conclusions

CQDs type significantly affects the glass transition temperature (CQDsRA-4 > CQDsRA-1 > CQDsRA-2 > CQDsRA-3) and optical properties of CQDsRA, while slightly influencing molecular movement, which follows a pyrometric cone trajectory. CQDs improve molecular compatibility, rheological properties, and aged asphalt regeneration. S or N doping reduces reflectivity, while O, N, S content significantly affects fluorescence. CQDs enhance RA fluorescence, whereas polycyclic aromatic hydrocarbons exhibit weak fluorescence inhibited by other asphalt components.

CRediT authorship contribution statement

Xin-Xing Zhou: Writing – review & editing, Writing – original draft, Resources, Funding acquisition, Conceptualization. **Tian-Qi Zong:** Writing – review & editing, Writing – original draft. **Ling-Lin Li:** Writing – review & editing. **Seung-Soo Kim:** Writing – review & editing.

Declaration of competing interest

The authors declare that they have no known competing financial interests or personal relationships that could have appeared to influence the work reported in this paper.

Acknowledgments

This work was supported by the National Natural Science Foundation of China (Nos. W2421062 and 52378456), Shanxi Province Sanjin Youth Top Talent Project (No. SJYC2024308), and Taiyuan City's Task-Assignment and Responsibility- Assignment Project (2025TYJB14).

References

Chen, H., Wen, K., Chen, J., et al., 2020. Ultra-stable tellurium-doped carbon quantum dots for cell protection and near-infrared photodynamic application. Sci. Bull. (Taipei) 65 (18), 1580–1586. https://doi.org/10.1016/j.scib.2020.05.021.

Dai, C., Wan, S., Li, Z., et al., 2024. Switchable unidirectional emissions from hydrogel gratings with integrated carbon quantum dots. Nat. Commun. 15, 845. https://doi.org/10.1038/s41467-024-45284-1.

Glattke, T., Chacon-Patino, M., Hoque, S., et al., 2022. Complex mixture analysis of emerging contaminants generated from coal tar- and petroleum-derived pavement sealants: molecular compositions and correlations with toxicity revealed by Fourier transform ion cyclotron resonance mass spectrometry. Environ. Sci. Technol. 56, 12988–12998.

Guo, S., Yang, Y., Liu, N., et al., 2016. One-step synthesis of cobalt, nitrogen-codoped carbon as nonprecious bifunctional electrocatalyst for oxygen reduction and evolution reactions. Sci. Bull. (Taipei) 61, 68–77. https://doi.org/10.1007/s11434-015-0978-6.

Guo, H., Lu, Y., Lei, Z., et al., 2024. Machine learning-guided realization of full-color high-quantum-yield carbon quantum dots. Nat. Commun. 15, 4843. https://doi.org/10.1038/s41467-024-49172-6.

He, Z., Xie, T., Yu, H., et al., 2023. Evaluation of quantum dot composite graphene-/Titanium oxide enhanced UV aging resistance modified asphalt. Constr. Build. Mater. 408, 133732. https://doi.org/10.1016/j.conbuildmat.2023.133732.

Humes, M., Machesky, J., Kim, S., et al., 2023. Primary and secondary organic aerosol formation from asphalt pavements. Environ. Sci. Technol. 57, 20034–20042.

Jalilov, A., Li, Y., Kittrell, C., et al., 2017. Increased CO_2 selectivity of asphalt-derived porous carbon through introduction of water into pore space. Nat. Energy 2, 932–938. https://doi.org/10.1038/s41560-017-0030-y.

Li, D., Leng, Z., Yao, L., et al., 2024a. Mechanical, economic, and environmental assessment of recycling reclaimed asphalt rubber pavement using different rejuvenation schemes. Resour. Conserv. Recycl. 204, 107534. https://doi.org/10.1016/j.resconrec.2024.107534.

Li, T., Xu, H., Teng, S., et al., 2024b. Modeling 0.6 million genes for the rational design of functional cis-regulatory variants and de novo design of cis-regulatory sequences. Proc. Natl. Acad. Sci. USA 121, e2319811121. https://doi.org/10.1073/pnas.2319811121.

Luo, J., Liu, X., Gu, J., et al., 2024. Construction of novel g-C_3N_4/β-FeOOH Z-Scheme heterostructure photocatalyst modified with carbon quantum dots for efficient degradation of RhB. J. Mater. Sci. Technol. 181, 11–19. https://doi.org/10.1016/j.jmst.2023.10.006.

Niles, S., Chacon-Patino, M., Putnam, S., 2020. Characterization of an asphalt binder and photoproducts by Fourier transform ion cyclotron resonance mass spectrometry reveals abundant water-soluble hydrocarbons. Environ. Sci. Technol. 54 (14), 8830–8836. https://doi.org/10.1021/acs.est.0c02263.

Ren, S., Liu, X., Erkens, S., 2024. Role of thermodynamic relaxation on effectiveness of recycling agents on properties of aged bitumen. Fuel 368, 131658. https://doi.org/10.1016/j.fuel.2024.131658.

Sarkar, H., Jagar, A., Abbas, K., 2026. Green-synthesized zinc quantum dots from parsley leaves for enhanced oil recovery: improving IFT, wettability, and oil recovery performance. Pet. Sci. 23 (6), 3519–3538. https://doi.org/10.1016/j.petsci.2026.02.017.

Schneider, F., Ortiz, J., Vanos, J., et al., 2023. Evidence-based guidance on reflective pavement for urban heat mitigation in Arizona. Nat. Commun. 14, 1467. https://doi.org/10.1038/s41467-023-36972-5.

Stokstad, E., 2020. It's not just cars that make pollution. It's the roads they drive on, too. Science News. 3 Sep 2020. https://doi.org/10.1126/science.abe6356.

Tian, S., Yang, D., Wu, Y., et al., 2025. Molecular dynamics simulation of pyrolysis in polyethylene cable sheaths under electric field. Prog. React. Kinet. Mech. 50, e019. https://doi.org/10.48130/prkm-0025-0018.

Wang, R., Fan, H., Jiang, W., et al., 2019. Amino-functionalized graphene quantum dots prepared using high-softening point asphalt and their application in Fe^{3+} detection. Appl. Surf. Sci. 468, 446–455. https://doi.org/10.1016/j.apsusc.2018.10.104.

Wang, Z., Wiedenhofer, D., Stephan, A., et al., 2022. High-resolution mapping of material stocks in belgian road infrastructure: material efficiency patterns, material recycling potentials, and greenhouse gas emissions reduction opportunities. Environ. Sci. Technol. 56, 12988–12998. https://doi.org/10.1021/acs.est.2c08703.

Wang, K., Cline, P., Schwan, J., et al., 2023. Efficient photon upconversion enabled by strong coupling between silicon quantum dots and anthracene. Nat. Chem. 15, 1172–1178. https://doi.org/10.1038/s41557-023-01225-x.

Wu, Y., Zheng, Y., Mu, J., et al., 2025. Biomass-derived amphiphilic nitrogen-doped carbon dots: molecular design, interfacial regulation, and enhanced oil recovery performance. Pet. Sci. 23 (4), 2046–2065. https://doi.org/10.1016/j.petsci.2025.12.011.

Xiao, F., Xu, L., et al., 2023. Recent applications and developments of reclaimed asphalt pavement in China, 2010-2021. Sustain. Mater. Technol. 37, e00697. https://doi.org/10.1016/j.susmat.2023.e00697.

Xu, S., Tang, G., Pan, S., et al., 2024. Application of reactive rejuvenator in aged SBS modified asphalt regeneration: a review. Constr. Build. Mater. 421, 135696. https://doi.org/10.1016/j.conbuildmat.2024.135696.

Yi, J., Wang, Y., Pei, Z., 2023. Mechanisms and research progress on biological rejuvenators for regenerating aged asphalt: review and discussion. J. Clean. Prod. 422, 138622. https://doi.org/10.1016/j.jclepro.2023.138622.

Yu, T., Wang, J., Zhang, H., et al., 2024. Statistical analysis of aging microcharacteristics for asphalt binder AFM images based on neural network classification. Fuel 371, 132080. https://doi.org/10.1016/j.fuel.2024.132080.

Zhang, J., Peng, J., Song, A., et al., 2024. Secondary organic aerosol formation potential from vehicular non-tailpipe emissions under real-world driving conditions. Environ. Sci. Technol. 58, 5419–5429. https://doi.org/10.1021/acs.est.3c06475.

Zhang, Z., Zhou, X., Wang, H., et al., 2025. The inhibition mechanism of VOCs and heavy metals in carbon dots synthesis wastewater. Process Saf. Environ. Prot. 204, 108149. https://doi.org/10.1016/j.psep.2025.108149.

Zhou, X., Chen, M., Wu, S., et al., 2024. Heavy metals and PAHs adsorption characteristics of bio-asphalt in road runoff. J. Clean. Prod. 450, 141923. https://doi.org/10.1016/j.jclepro.2024.141923.